# NUMERICAL PREDICTIONS OF CRYOGENIC HYDROGEN VERTICAL JETS

**Giannissi, S.G.[1,*], Venetsanos, A.G.[1] and Hecht, E.S.[2]**
**[1] Environmental Research Laboratory, National Center for Scientific Research Demokritos, Aghia Paraskevi, Athens, 15341, Greece, sgiannissi@ipta.demokritos.gr, venets@ipta.demokritos.gr**
**[2] Combustion Research Facility, Sandia National Laboratories, P.O. Box 969, MS 9052, Livermore, CA, 94551, USA, ehecht@sandia.gov**

## ABSTRACT

Comparison of CFD predictions with measurements is presented for cryo-compressed hydrogen vertical jets. The stagnation conditions of the experiments are characteristic of unintended leaks from pipe systems that connect cryogenic hydrogen storage tanks and could be encountered at a fuel cell refueling station. Jets with pressure up to 5 bar and temperatures just above the saturation liquid temperature were examined. Comparisons are made to the centerline mass fraction and temperature decay rates, the radial profiles of mass fraction and the contours of volume fraction. Two notional nozzle approaches are tested to model the under-expanded jet that was formed in the tests with pressures above 2 bar. In both approaches the mass and momentum balance from the throat to the notional nozzle are solved, while the temperature at the notional nozzle was assumed equal to the nozzle temperature in the first approach and was calculated by an energy balance in the second approach. The two approaches gave identical results. Very good agreement with the measurements was found in terms of centerline mass fraction and temperature for all tests except for the test with 3 bar release where concentration was overpredicted. Furthermore, a wider radial spread was observed in the predictions possibly revealing higher degree of diffusion using the k-ε turbulence model. An integral model for cryogenic jets was also tested and provided good results. Finally, a test simulation was performed with an ambient temperature jet and compared to the cold jet and showed that warm jets are faster than cold jets.

Keywords: cryogenic, hydrogen, CFD, jet, integral model

## 1.0 INTRODUCTION

The prospects of a large fleet of fuel cell electric vehicles lead to the need to design and construct refueling stations. To have the necessary amount of hydrogen on-site and an efficient distribution, hydrogen is likely to be stored and transported as a liquid due to its high density (relative to compressed gas). Cryo-compressed hydrogen is a method for storage and transportation of hydrogen. Cryo-compressed hydrogen can be in vapor, liquid or supercritical state inside the tank.

To study the behavior of cryo-compressed hydrogen in case of an accidental leak, release and dispersion experiments have been performed in the past with high reservoir pressures up to 32 bar and low temperatures reaching 34 - 80 K. The release was in stagnant environment. A brief review on cryo-compressed experiments that have been performed in the past can be found in [1] and [2]. Most of the experiments with dispersion of cryo-compressed hydrogen involve horizontal releases.

Recently, experiments have been conducted by Sandia National Laboratories with upward vertical release of cryo-compressed hydrogen [2] to simulate leak scenarios from a cryogenic hydrogen storage system. The reservoir temperature was in the range of 50-61 K and the reservoir pressure was 2-5 bar. Two nozzle diameters were tested, 1 mm and 1.25 mm. The scope of these experiments was to provide a series of data with controlled release conditions and large spatial resolution suitable for quantitative model validation for releases at temperatures below 80 K. The successfully validated models will be able to perform risk and safety analyses, in order to provide a scientific basis to justify the

modification of separation distances that NFPA 2: Hydrogen Technologies Code [3] prescribes for liquid hydrogen.

Previous work of the authors [1] that simulated horizontal cryogenic hydrogen jets using Computational Fluid Dynamics (CFD) showed good agreement with the respective measurements. The experiments that were simulated had stagnation conditions that correspond to vapor and supercritical state.

In the present work, the vertical cryogenic hydrogen jets studied by Sandia [2] are simulated. The reservoir conditions correspond to the vapor phase. The tests with release through 1 mm nozzle are chosen for this study. In contrast to the previous CFD work of the authors, where only the centerline concertation predictions were compared to experiments, in this study the rate of hydrogen dispersion radially is also presented and compared with the experiments. Normalized temperature decay rate and volume fraction contours are also produced and compared with the respective experimental data. Finally, an integral model based on [4] and [5] has been developed and the results for the Sandia experiments with 1 mm nozzle are presented and evaluated.

## 2.0 THE SANDIA EXPERIMENTS

The detailed experimental description can be found in [2] and [6]. Briefly, 9 hydrogen experiments are reported with 4 releases through a 1 mm nozzle and 5 releases through a 1.25 mm nozzle. The reservoir conditions were varied from 2-5 bar pressure and 50-61 K (see Table 1). The release was vertically upward. During the experiments, a low intensity co-flow of air (0.3 m/s) surrounded the jet to minimize the effect of any room currents. Planar laser Raman imaging measurements enabled the calculation of concentration (mole fractions) and temperatures in two dimensions.

## 3.0 MODELLING APPROACH

The experiments with release through 1 mm nozzle were simulated using both CFD and an integral model. In the following Sections, details about each methodology can be found.

### 3.1 CFD methodology

For the CFD simulations the 3D time dependent conservation equations (1)-(4) were solved using the ADREA-HF code.

$$\frac{\partial \rho}{\partial t} + \frac{\partial \rho u_i}{\partial x_i} = 0 \tag{1}$$

$$\frac{\partial \rho u_i}{\partial t} + \frac{\partial \rho u_i u_j}{\partial x_j} = -\frac{\partial P}{\partial x_i} + \frac{\partial}{\partial x_j}\left( (\mu + \mu_t)\left( \frac{\partial u_i}{\partial x_j} + \frac{\partial u_j}{\partial x_i} \right) \right) + \rho g_i \tag{2}$$

$$\begin{aligned} \frac{\partial \rho h}{\partial t} + \frac{\partial \rho u_i h}{\partial x_i} = \frac{dP}{dt} + \frac{\partial}{\partial x_i}\left( (\lambda + \lambda_t)\frac{\partial T}{\partial x_i} \right) \\ + \frac{\partial}{\partial x_i}\left( \rho \sum_{k \neq a} D_{q_k}\left( h_{v_k} - h_{v_a} \right)\frac{\partial q_{v_k}}{\partial x_i} \right) + \frac{\partial}{\partial x_i}\left( \sum_k \frac{\mu_t}{Sc_t} h_k \frac{\partial q_k}{\partial x_i} \right) \end{aligned} \tag{3}$$

$$\frac{\partial \rho q_p}{\partial t} + \frac{\partial \rho u_j q_p}{\partial x_j} = \frac{\partial}{\partial x_j}\left( \left( \rho D_p + \frac{\mu_t}{Sc_t} \right)\frac{\partial q_p}{\partial x_j} \right) \tag{4}$$

where $\rho$ - mixture density, kg/m$^3$; P - pressure, Pa; T - temperature, K; $\mu$, $\mu_t$ - laminar and turbulent viscosity respectively, kg/m/s; $\lambda$, $\lambda_t$ - laminar and turbulent thermal conductivity respectively, W/m/K; $Sc_t$ - turbulent Schmidt number, dimensionless; D - molecular diffusivity, m$^2$/s; h - enthalpy, J/kg; q - total mass fraction (vapor and liquid if it exists). The turbulent Schmidt number is set equal to 0.72. The subscripts i and j denote the Cartesian x, y and z coordinates, index p denotes the component p, index v is for the vapor phase and index a is for air. For turbulence modelling the k-ε model with extra buoyancy terms was used.

Initial simulations that included the co-flow of air showed little sensitivity on the results due to the low air velocity (0.3 m/s) and therefore it was neglected.

For the discretization of the convective terms in the momentum, the enthalpy and the mass fraction equations, a 2$^{nd}$ order numerical scheme (the MUSCL) was applied. For time integration, a 1$^{st}$ order numerical scheme was used and for the diffusive terms, central differences were applied. An under-relaxation factor equal to 0.7 was imposed in all variables. A maximum CFL number equal to 10 was set in tests with reservoir pressure 2, 3 and 4 bar and 1 for the test with 5 bar to restrict the maximum time step and for convergence stability. Larger CFL number in test with 5 bar led to convergence issues, i.e. more internal iterations were required and the time step was decreased until CFL was approximately equal to 1.

Due to the high reservoir pressure, the throat can remain at higher than ambient pressure and, consequently, form an under-expanded jet downwind from the nozzle. As Table 1 indicates for the tests with reservoir pressure higher than 2 bar, this is the case, while for the jet with 2 bar release the pressure at the throat was found equal to ambient (0.972 bar). The calculations were made assuming isentropic expansion from storage to throat conditions using the HEM critical flow model presented in [1]. The results agree perfectly with the ones presented in [6].

The under-expanded jet was modeled using two approaches: the approach that solves the mass and momentum balance from the throat to the notional nozzle assuming that the temperature at the notional nozzle is equal to the throat temperature [1], and the approach that solves the mass, momentum and energy balance from the throat to the notional nozzle similar to [7] and [8] but using the NIST equation of state. For the test with 2 bar release such calculations are not necessary since no under-expanded jet is formed.

Table 1 shows the predicted conditions at the notional nozzle by the two approaches for the tests that were simulated in the present study. With the second approach lower temperatures were predicted in notional nozzle and the higher the stagnation pressure the higher the temperature difference from the first approach. This also results in smaller notional diameter to conserve the mass flow rate.

In previous work of the authors [1], the first approach was used and showed in general good agreement with the measurements. However, the second approach was not tested, because in those experiments, the isentropic energy balance resulted in saturation temperatures where two-phase flow occurred at the notional nozzle, increasing the complexity of the CFD simulations. In the experiments studied here, the temperature does not fall below the saturation temperature, as shown in Table 1, and single phase is predicted at the notional nozzle. Therefore, both approaches were tested. Comparison between the two approaches showed that the predicted concentrations were identical. Thus, for space economy the dispersion results using only the second approach (solving the mass, momentum and energy balance) are presented.

Table 1. Stagnation conditions, throat conditions, notional nozzle conditions with two notional approaches.

| Stagnation | | | Throat | | | Notional nozzle | | | | | |
|---|---|---|---|---|---|---|---|---|---|---|---|
| | | | | | | Approach solving mass and momentum balance | | | Approach solving mass, momentum and energy balance | | |
| T (K) | P (bar) | D (mm) | T (K) | P (bar) | U (m/s) | T (K) | U (m/s) | D (mm) | T (K) | U (m/s) | D (mm) |
| 58 | 2 | 1 | 43.5 | 0.972 | 544.5 | 43.5 | 544.65 | 1 | 43.5 | 544.65 | 1 |
| 56 | 3 | 1 | 41.9 | 1.457 | 533.3 | 41.9 | 639.17 | 1.12 | 35.77 | 639.17 | 1.03 |
| 53 | 4 | 1 | 39.6 | 1.940 | 516.4 | 39.6 | 669.53 | 1.25 | 30.46 | 669.53 | 1.09 |
| 50 | 5 | 1 | 37.4 | 2.422 | 498.2 | 37.4 | 674.92 | 1.38 | 26.64 | 674.92 | 1.15 |

The computational domain for the CFD simulations was extended around the release point from -50 mm to 50 mm in the x direction, from 0 to 100 mm in the y direction, which symmetry was assumed and from 0 to 140 mm in the z-direction. The release point was set at (0, 0, 2 mm). Two cells were used to discretize the source. The expansion ratio was 1.05 in all direction close to the release and further downwind it was increased to a maximum value of 1.08. The total number of cells was 202,370 for the test with 2 and 3 bar pressure, 188,564 for test with 4 bar and 179,124 for test with 5 bar. Open boundary conditions were used in all planes except for the bottom plane where a wall boundary was imposed.

### 3.2 Integral model

An integral model was also developed and used in this study, in order to predict the cryogenic jet distribution. The integral model was based on the COLDPLUME model [9]. It is coded in Fortran and uses the properties package of ADREA-HF code.

The model distinguishes three regions for the cryogenic jet development: the under-expanded zone, the zone of flow establishment and the zone of established flow. The under-expanded zone is the region where the jet expands to ambient pressure. The notional nozzle approach, which solves the mass, momentum and energy balance, is employed to estimate the conditions at the end of that zone similar to the CFD simulations. The zone of flow establishment is characterized by the transformation of “plug flow” exiting the zone of under-expanded jet into the fully developed jet flow with Gaussian profiles for the velocity and the scalar transport quantities, which enters the zone of established flow. The exiting conditions of under-expanded zone are the entering boundary conditions for the zone of flow establishment. The model for the zone of flow establishment that is described in [9] is also used here.

Winters [9] describe another region after the under-expanded zone and before the zone of flow establishment, the zone of initial entrainment and heating. This zone is recommended for cryogenic jets, because the temperature at the end of the under-expanded zone is quite cold and a two-phase mixture is likely to occur. To avoid such complexity, it is assumed that air entrains the jet and warms it up to 47 K. This temperature is arbitrary chosen, so as the REFPROP package that is used by COLDPLUME can characterize the state for the exiting air and hydrogen mixture [5]. In the present study, this zone is omitted. The ADREA-HF properties package had no issues calculating the properties of these cryogenic mixtures. Tests including the zone of initial entrainment and heating using the ideal gas equation of state gave no improvement in the results. In fact, they were in less agreement with the experiment for most of the experiments.

In the zone of established flow the velocity, the density and the mass fraction have Gaussian profiles and take the following forms,

$$U = U_{CL} \exp\left(\frac{-r^2}{B^2}\right) \tag{5}$$

$$\rho = \rho_a + (\rho_{CL} - \rho_a)\exp\left(\frac{-r^2}{\lambda^2 B^2}\right) \tag{6}$$

$$\rho Y = \rho_{CL} Y_{CL} \exp\left(\frac{-r^2}{\lambda^2 B^2}\right) \tag{7}$$

where Y - the hydrogen mass fraction, B - the radius of the jet boundary, r - the radial coordinate and $\lambda$ represents the relative spreading ratio between velocity and scalar properties and was set equal to 1.16 as in [5]. The index CL is for the centerline conditions. Through cross-sectional integration and assuming the Gaussian profiles, the variables for the total mass, M, the axial momentum flux, $M_v$, the released substance's mass fraction, Q, and the total energy, E, are obtained,

$$M = \int_0^{2\pi}\int_0^{\infty} \rho U r dr d\theta = \pi\left(B^2 U_{CL}\left(\rho_a - (\rho_a - \rho_{CL})\frac{\lambda^2}{\lambda^2+1}\right)\right) \tag{8}$$

$$M_v = \int_0^{2\pi}\int_0^{\infty} \rho U^2 r dr d\theta = \frac{\pi}{2}\left(B^2 U_{CL}^2\left(\rho_a - (\rho_a - \rho_{CL})\frac{2\lambda^2}{2\lambda^2+1}\right)\right) \tag{9}$$

$$Q = \int_0^{2\pi}\int_0^{\infty} \rho U Y r dr d\theta = \pi \rho_{CL} Y_{CL} U_{CL} B^2 \frac{\lambda^2}{\lambda^2+1} \tag{10}$$

$$E = \int_0^{2\pi}\int_0^{\infty} \rho U\left(h + \frac{1}{2}U^2 - h_{amb}\right) r dr d\theta \tag{11}$$

where $\theta$ is the angle between the jet centerline and the horizontal. The conservation equations of flux quantities along the jet centerline, s, defined by eq. (8)- (11), are the followings,

$$\frac{dM}{ds} = \rho_a Entrain \tag{12}$$

$$\frac{dM_v \cos\theta}{ds} = 0 \tag{13}$$

$$\frac{dM_v \sin\theta}{ds} = \int_0^{2\pi}\int_0^{\infty} (\rho_a - \rho) g r dr d\theta \tag{14}$$

$$\frac{dQ}{ds} = 0 \tag{15}$$

$$\frac{dE}{ds} = 0 \tag{16}$$

where Entrain is the rate of entrainment. Combining eq. (13) and (14) we get the following system of equations,

$$\frac{dM}{ds} = \rho_a \text{Entrain} \tag{17}$$

$$\frac{dM_v}{ds} = \pi\lambda^2 B^2 g\left(\rho_a - \rho_{CL}\right)\sin\theta \tag{18}$$

$$\frac{d\theta}{ds} = \frac{\pi\lambda^2 B^2 g\left(\rho_a - \rho_{CL}\right)\cos\theta}{M_v} \tag{19}$$

$$\frac{dQ}{ds} = 0 \tag{20}$$

$$\frac{dE}{ds} = 0 \tag{21}$$

We have two additional differential equations by relating s, $\theta$, x and y,

$$\frac{dx}{ds} = \cos\theta \tag{22}$$

$$\frac{dy}{ds} = \sin\theta \tag{23}$$

The set of eq. (17)-(23) yield to a system of ordinary differential equations. To solve the system additional equations are required that relate the variables, M, $M_v$, E, Q, $U_{CL}$, $Y_{CL}$, $\rho_{CL}$, $\theta$ and B. Using the ideal mixture density and after several calculations, we extract 4 extra algebraic equations,

$$\rho_{CL} = \frac{\rho_a \frac{Q}{M}\left(\frac{1}{\rho_{H_2}} - \frac{1}{\rho_a}\right)\left(1 - \frac{\lambda^2}{\lambda^2+1}\right) - \frac{\lambda^2}{\lambda^2+1}}{-\frac{1}{\rho_a}\frac{\lambda^2}{\lambda^2+1} - \frac{Q}{M}\left(\frac{1}{\rho_{H_2}} - \frac{1}{\rho_a}\right)\frac{\lambda^2}{\lambda^2+1}} \tag{24}$$

$$U_{CL} = 2\frac{M_v}{M}\frac{\left[\left(\rho_a - \left(\rho_a - \rho_{CL}\right)\frac{\lambda^2}{\lambda^2+1}\right)\right]}{\left(\rho_a - \left(\rho_a - \rho_{CL}\right)\frac{2\lambda^2}{2\lambda^2+1}\right)} \tag{25}$$

$$B = \sqrt{\frac{M}{U_{CL}\pi\left(\rho_a - \left(\rho_a - \rho_{CL}\right)\frac{\lambda^2}{\lambda^2+1}\right)}} \tag{26}$$

$$Y_{CL} = \frac{Q}{\pi\rho_{CL}U_{CL}B^2\frac{\lambda^2}{\lambda^2+1}} \tag{27}$$

Eq. (17)-(27) constitutes a system of 11 differential-algebraic equations (DAEs) with unknowns the variables: x, y, M, $M_v$, Q, E, $U_{CL}$, $Y_{CL}$, $\rho_{CL}$, B, $\theta$. The system is solved numerically using the Runge-Kutta 4$^{th}$ order method. For the density at the jet centerline, $\rho_{CL}$, the enthalpy and hydrogen mass fraction at the jet centerline, $h_{CL}$ and $Y_{CL}$, respectively, are required. The enthalpy is derived from the total energy, E. The expression for the energy (11) is complicated and cannot be calculated in a straightforward manner, thus, to derive E we use an iterative method. We iterate on temperature at jet centerline, $T_{CL,}$ assuming constant pressure equal to ambient and we solve eq. (24)-(27) until E is equal to $E_0$ (the energy at the end of flow of establishment). For each temperature, the phase distribution of hydrogen is calculated using a PTFLASH algorithm in case two-phase conditions occur. The integral (11) for the calculation of E is solved numerically using the trapezoidal rule and the upper integration limit is replaced by 3B. From this process, we estimate also the temperature at the jet centerline.

To close the system of equations a model for the air entrainment is also required. The general form of the entrainment model is,

$$\text{Entrain} = 2\pi \text{B}\alpha \text{U}_{\text{CL}} \tag{28}$$

where $\alpha$ - the local mass entrainment coefficient. This coefficient takes different values if we have jet or plume. There are different entrainment models in literature that differ mainly in the entrainment coefficient that they use. Some models use a specific value, which is typically empirically determined, while others use an equation to estimate the local mass entrainment coefficient based on Froude number [4]. In hydrogen applications, where buoyancy plays an important role, Xiao et al. [8] uses an equation that takes into account the transition from jet to plume based on the Richardson number, while Houf et al. [5] and [10] distinguish two components of rate of entrainment, one due to exit momentum and one due to buoyancy. The momentum component is constant and depends on the release conditions, while the buoyancy component is given by $\text{E}_{\text{buo}} = 2\pi \text{B}\alpha \text{U}_{\text{CL}} \sin(\theta)/\text{Fr}$ using a correlation for coefficient, α, that gives the best results based on vertical ambient hydrogen jet experiments [10].

In the present study, we use the following relation, which is a combination of the relations presented in [4] and [8],

$$\alpha = 2\pi \text{BU}_{\text{CL}} \left( \alpha_1 + (\alpha_2 - \alpha_1) \frac{\sin(\theta)}{\text{Fr}} \right) \tag{29}$$

where $\alpha_1$=0.055 for pure jet, $\alpha_2$=0.085 for pure plume and $\text{Fr} = \dfrac{\text{U}_{\text{CL}}^2}{\left| \text{gB}(\rho_{\text{amb}} - \rho_{\text{CL}})/\rho_{\text{release}} \right|}$. The first term is for the pure jet and the second term is for the transition from jet to plume.

For the DAEs system to be well defined, boundary conditions at the beginning of the jet should be given. For the zone of established flow as inlet boundary conditions, the conditions exiting the zone of flow establishment are imposed.

Finally, in all zones the properties of ideal gas are used except for the under-expanded zone where the NIST EoS is used due to the high pressures that occur in that zone. Appropriate changes have been made in the diameter of the jet at the end of the under-expanded zone, so that mass is conserved when using the ideal gas density in the zone of flow establishment.

## 4.0 RESULTS AND DISCUSSION

### 4.1 Comparison with experiment

#### 4.1.1 CFD results

Figure 1 shows the inverse mass fraction and the normalized inverse temperature decay rate along the jet centerline for the CFD simulation of all tests compared to the respective experimental data. The z axis is normalized as $\zeta = \frac{z}{d_{nozzle}\sqrt{\rho_{throat}/\rho_a}}$, where $\rho_{throat}$ is the density at the throat as computed assuming isentropic expansion (see Section Modelling approach) and $\rho_a$ is the density of ambient air (about 1.18 kg/m$^3$). In [2], a different normalization was applied using the reservoir density instead of the throat density. However, the throat density is considered a more typical normalization parameter for our case.

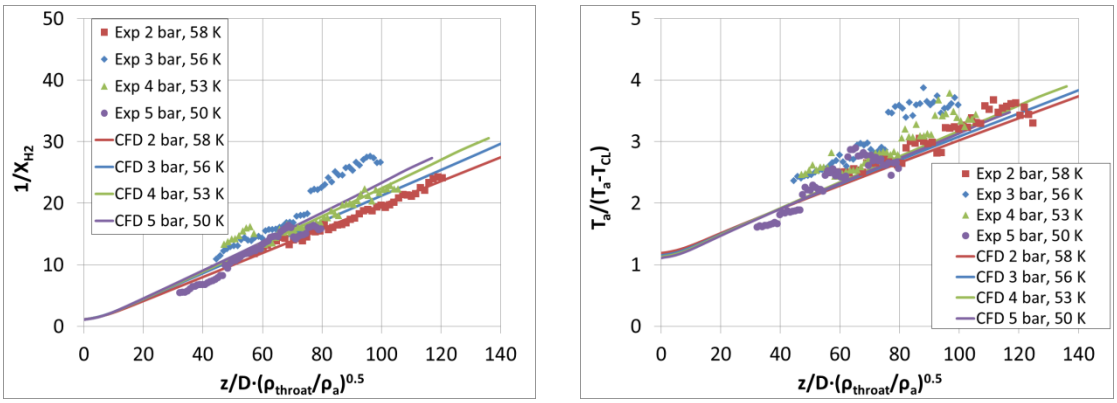


Figure 1. Comparison of CFD results with experiment for all the tests with 1mm diameter, right: temperature, left: mass fraction.

The decay rates of both concentration and temperature indicate a fairly good agreement with the experiment for all tests except for test at 3 bar, where the mass fraction is overpredicted and the temperature is underpredicted. This behavior indicates that in the experiment the jet was warmer than in the simulation. In [2], it is noted that ice growth on the nozzle can cause the jet to shift from the centerline. This may have been especially prevalent for the 3 bar release. This shift from the centerline could be the reason for the larger discrepancies between prediction and experiment for this release case.

Another reason for the higher experimental temperatures could be attributed to the freezing of air components and ambient humidity. However, based on [11] the air components freezing effect is negligible in cryo-compressed releases similar to the examined case due to the fact that it occurs only at a small region close to the nozzle where jet momentum dominates. Simulations of 2 bar and 3 bar release that took into account the condensation/freezing effect of nitrogen and oxygen (with the same modelling approach as in [11]) verified that there was no actual effect on the concentration and that the temperature was slightly higher (~ 2K) very close to the nozzle in the case with air freezing. The humidity effect is also negligible for jets with densimetric release Froude number (Fr) above 1000 according to [11]. In the examined jets, the densimetric Fr number ranges from 5445 to 28688, values way above the critical value of 1000. Therefore, it is safe to assume that a simulation with humidity would not affect the results.

The predicted normalized radial mass fraction profiles presented in Figure 2 show a satisfactory agreement with the experiment in all tests. However, predictions tend to give less spreading at z/d=59 in the test with 3 bar release and in general more spreading in the test with 5 bar release.

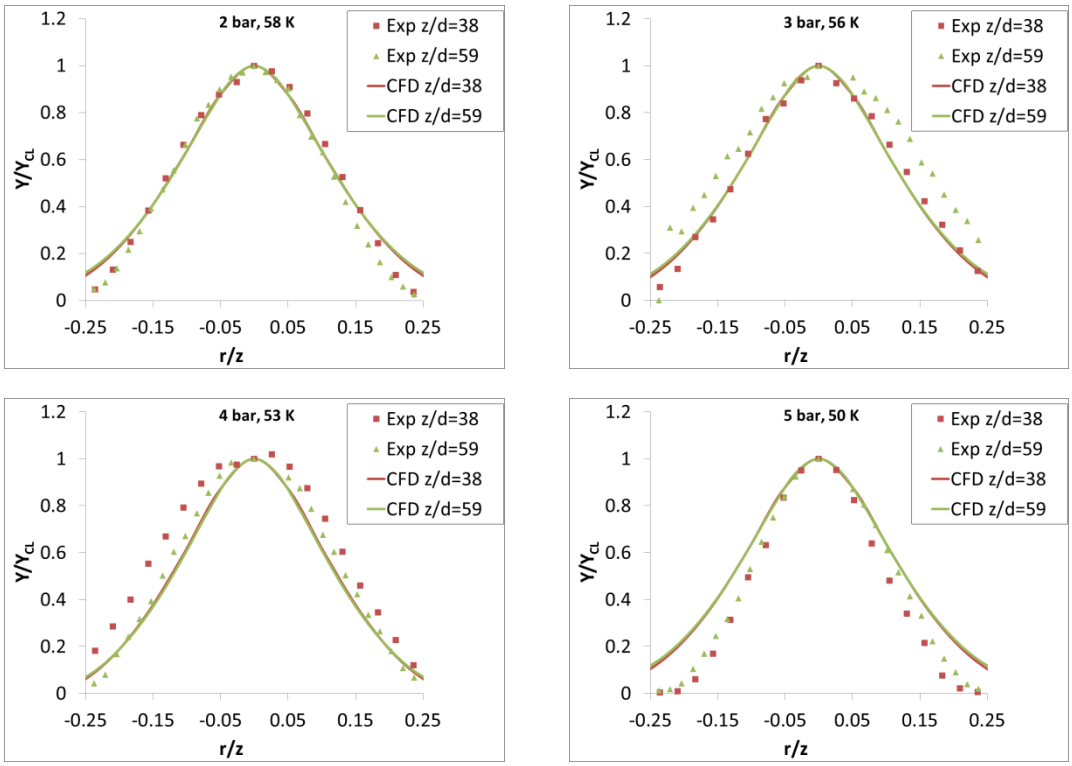


Figure 2. Comparison of radial mass fractions at selected distances, normalized by the centerline mass fraction between the CFD simulation and the experiment.

Finally, Figure 3 illustrates the volume fraction contours of the CFD simulations (flood) along with the respective experimental contours (lines) for the four tests. It is obvious that as we move away from the release the simulations predicted more lateral spreading. This is more evident in 5 bar release experiment, as was already mentioned based on the figure with the radial mass fractions (Figure 2). A possible reason for that behavior could be an overprediction of the turbulent diffusion computed by the k-ε model that was used for the turbulence modeling.

2 bar, 58 K

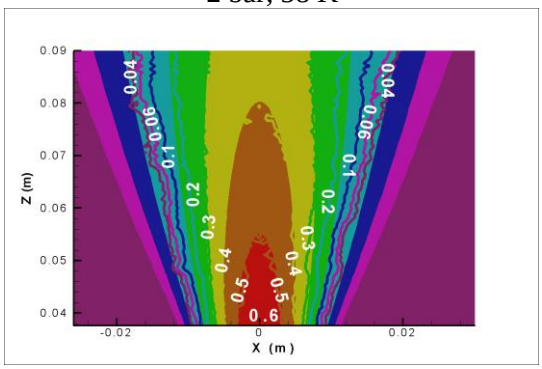


3 bar, 56 K

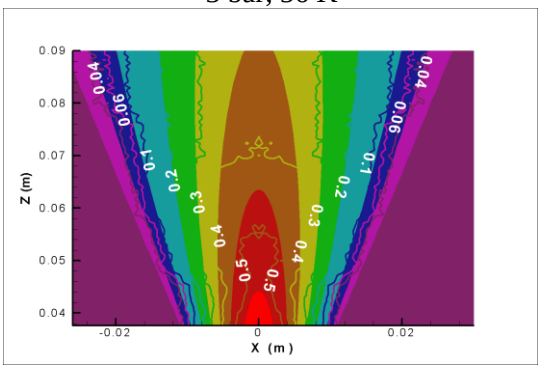

4 bar, 53 K

5 bar, 50 K

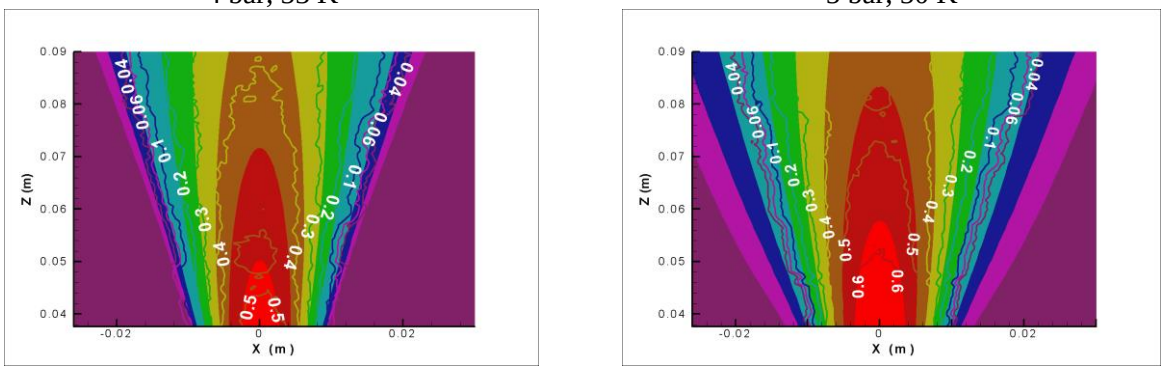


Figure 3. The volume fraction contours of CFD simulations (flood) and experiments (lines).

### 4.1.2 Integral model results

Figure 4 displays the inverse mass fraction and the normalized inverse temperature decay rate along the jet centerline for the integral model along with the respective experimental data. The results are in very good agreement with the experiment. With the normalization that we used both the concentration and the temperature decay rates almost coincide for the 4 tests. Small discrepancies between the model predictions and the experiment are observed for the test with 3 bar release for the same reasons mentioned in Section CFD results.

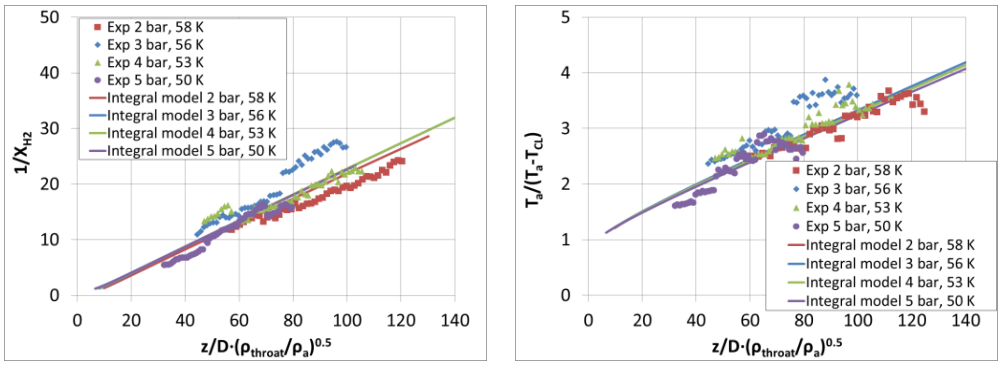


Figure 4. Comparison of integral model results with experiment for all the tests with 1mm diameter, right: temperature, left: mass fraction.

Figure 5 displays the volume fraction contours of the integral model (flood) along with the respective experimental contours (lines) for the four tests. We observe that the volume fraction profiles are well predicted and that the lateral spreading is predicted better than in CFD simulations.

2 bar, 58 K

3 bar, 56 K

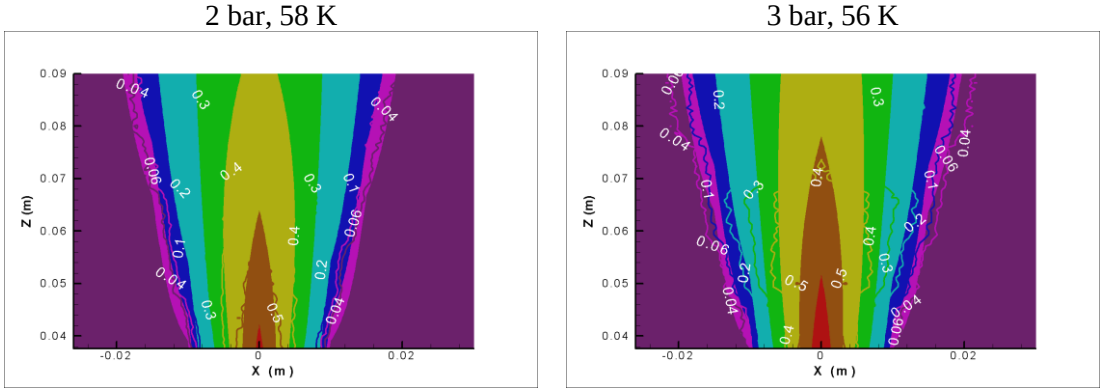

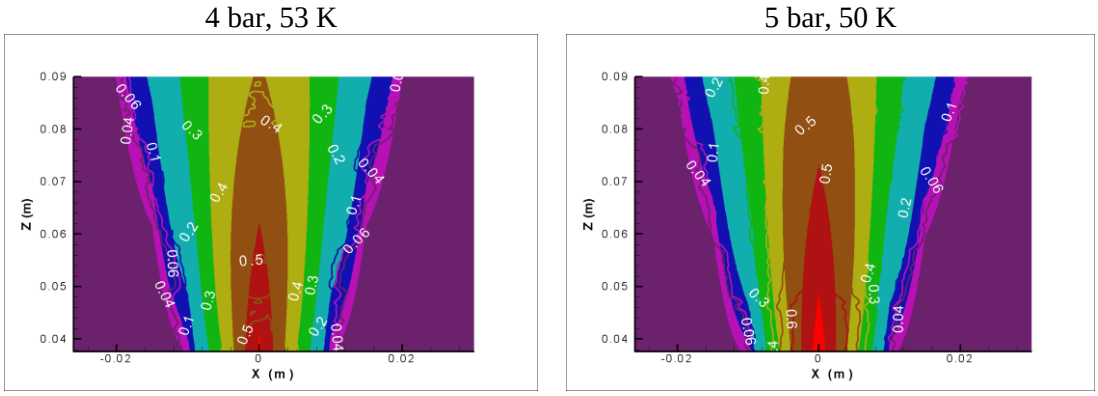


Figure 5. The volume fraction contours of integral model predictions (flood) and experiments (lines).

### 4.2 Comparison with ambient jets

In [2], it is mentioned that for warm jets (ambient reservoir temperature) the half-width decay rate is faster than the cryogenic jets and in order for the centerline mass fraction decay rate to be similar to, and mass to be conserved, the velocity should also be higher. To check this we performed an additional simulation similar to the experiment with 2 bar release, but with ambient reservoir temperature. All other characteristics were kept the same. The mass flux and the conditions at the throat were calculated using the HEM critical flow model similar to the cryogenic simulations.

Figure 6 shows the predicted concentration decay rate (left) and the inverse velocity (right) for the warm and the cold jet. It can be observed that the concentration decay rate is the same, while the velocity decay is different. More precisely, the velocity decay in warm jets faster than in cold jets, i.e. warm jets are faster than cold jets.

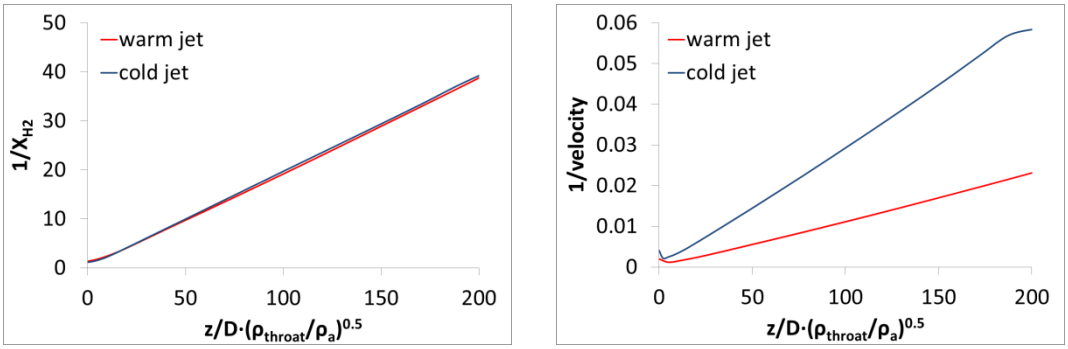


Figure 6. Comparison between warm and cold jets.

## 5.0 CONCLUSIONS

Four simulations of cryogenic hydrogen jets were performed based on experiments conducted by Sandia National Laboratories using CFD and an integral model. In the Sandia experiments that were simulated here, hydrogen was released vertically upwards through a 1 mm nozzle. The reservoir pressure was varied from 2-5 bar and the reservoir temperature was between 50-58 K. For the tests with release pressure above 2 bar, an underexpanded jet formed, which was modelled with the help of the notional nozzle approach that solves the mass, momentum and energy balance from the throat to the point where pressure is reduced to ambient (the notional nozzle). The conditions at the throat were computed assuming isentropic expansion from the reservoir conditions.

Generally, good agreement was found between the concentration and temperature predictions along the jet centerline with the experiment by both CFD and the integral model. However, a tendency to

overpredict the mass fraction and underpredict the temperature was found for the 3 bar release conditions. This is likely due to the icing around the nozzle, which shifts the release laterally, a phenomenon which was most prevalent for the 3 bar release.

The CFD model predicted more lateral spreading compared to the experiments, as the radial mass fraction profiles and the volume fraction contours indicate. The k-ε model used for the turbulence modeling might be the reason for this discrepancy, and might require adjustment (reduction) to accurately predict cryogenic dispersion. On the other hand, the integral model predicts the two-dimensional volume fraction fields that are in better agreement with the experiments than the CFD model.

Finally, with the help of CFD simulations it was shown that the centerline mass fraction decay rate is similar for warm jets (ambient reservoir temperature) and cold jets, but the velocity decay is faster for warm jets, as was suggested in [2].

## 6.0 ACKNOWLEDGMENTS

The research leading to these results was financially supported by the PRESLHY project, which has received funding from the Fuel Cells and Hydrogen 2 Joint Undertaking under the European Union's Horizon 2020 research and innovation programme under grant agreement No 779613.

Sandia National Laboratories is a multi-mission laboratory managed and operated by National Technology and Engineering Solutions of Sandia LLC, a wholly owned subsidiary of Honeywell International Inc. for the U.S. Department of Energy's National Nuclear Security Administration under contract DE-NA0003525. This paper describes objective technical results and analysis. Any subjective views or opinions that might be expressed in the paper do not necessarily represent the views of the U.S. Department of Energy or the United States Government.

## REFERENCES

[1] Venetsanos, A.G. and Giannissi, S.G., Release and dispersion modeling of cryogenic under-expanded hydrogen jets, *Int. J. Hydrogen Energy*, **42**, No. 11, 2017, pp. 7672–7682.

[2] Hecht, E.S. and Panda, P.P., Mixing and warming of cryogenic hydrogen releases, *Int. J. Hydrogen Energy*, **44,** No 17, 2019, pp. 8960–8970.

[3] NFPA 2: Hydrogen technologies code, Tech. Rep. National Fire Protection Association, 2016.

[4] Jirka, G.H., Integral Model for Turbulent Buoyant Jets in Unbounded Stratified Flows . Part I : Single Round Jet, *Environ. Fluid Mech.*, **4**, pp. 1–56, 2004.

[5] Houf, W.G. and Winters, W.S., Simulation of high-pressure liquid hydrogen, *Int. J. Hydrogen Energy*, **38**, No. 19, 2013, pp. 8092–8099.

[6] Panda, P.P. and Hecht, E.S., Ignition and flame characteristics of cryogenic hydrogen releases, *Int. J. Hydrogen Energy*, **42**, No. 1, 2016, pp. 775–785.

[7] Yüceil, K. and Ötügen, M., Scaling parameters for underexpanded supersonic jets, *Phys. Fluids*, **14**, No. 12, 2002, pp. 4206.

[8] Xiao, J., Travis, J.R. and Breitung, W., Hydrogen release from a high pressure gaseous hydrogen reservoir in case of a small leak, *Int. J. Hydrogen Energy*, **36**, No. 3, 2011, pp. 2545–2554.

[9] Winters, W.S., Modeling leaks from liquid hydrogen storage systems, Sandia National Laboratories Report No. SAND2009-0035.

[10] Houf, W. and Schefer, R. Analytical and experimental investigation of small-scale unintended releases of hydrogen, *Int. J. Hydrogen Energy*, **33**, No. 4, 2008, pp. 1435–1444.

[11] Giannissi, S.G. and Venetsanos, A.G., A comparative CFD assessment study of cryogenic hydrogen and LNG dispersion, *Int. J. Hydrogen Energy*, **44**, No. 17, 2019, pp. 9018–9030.